Extension and Application of a Local, Minimum Aliasing Method to Multidimensional Problems in Limited-Area Domains

JERRY M. STRAKA

School of Meteorology, University of Oklahoma—Norman, Norman, Oklahoma

JOHN R. ANDERSON

Department of Atmospheric and Oceanic Sciences, University of Wisconsin—Madison, Madison, Wisconsin

(Manuscript received 25 March 1992, in final form 22 March 1993)

ABSTRACT

The minimal aliasing local spectral (LS) method is a numerical technique that embodies features of both finite-difference (FD) and spectral transform (ST) methods. Anderson first described this method in the context of the one-dimensional advection–diffusion equation. In the current paper, we describe the extension of the LS method to multidimensions. First, we review the one-dimensional version of the LS method from a more rigorous view. In addition, we describe interpolation, differentiation, and dealiasing filters for the LS method based on Lagrange polynomials. Without the dealiasing filters, this version of the LS method collapses to a standard high-order Taylor series FD scheme. When filter lengths span the integration domain and the dealiasing stage is retained, the LS method becomes an ST method, as described by Anderson. Issues concerning the implementation of the LS method in multidimensions are also discussed. These issues include the form of the high-resolution grid, the implementation of the interpolation stage, and the implementation of the dealiasing stage. Then, we test the LS method with a two-dimensional nonlinear density current problem using idealized boundary conditions. Comparisons are made with a high-resolution reference solution from a reference model, as well as with solutions from a high-order FD model. Results from simulations of the test problem demonstrate that the LS method is more accurate than high-order FD schemes at coarse grid resolutions, and as accurate at finer grid resolutions. Furthermore, the results show that solutions from LS models are more robust than solutions from FD models. After this, we show that dealiasing the nonlinear advection tendencies plays an important role in the success of the LS method, especially for simulations with sharp boundaries that are marginally resolved. For adequately resolved flows, dealiasing does not necessarily improve solutions for the short-term integrations that are presented. However, aliasing errors still must be controlled to prevent a catastrophic buildup of energy at the smallest resolvable wavelengths. Finally, the LS method is tested using open lateral boundary conditions. As the LS method is a higher-order scheme, special treatment of the vertical and lateral boundaries is required. One possibility is to use lower-order versions of the LS method as boundaries are approached, and outflow conditions at the lateral boundaries. This simple treatment results in solutions that compare very favorably to the reference solution of the test problem.

1. Introduction

Aliasing errors are a potentially serious problem when finite-difference (FD) methods are used in grid-point models to integrate the Navier–Stokes equations for fluid flows (Phillips 1959). These errors are due to the production of unresolvable high spatial wavenumbers in the computation of the quadratic and higher-order product terms such as nonlinear advection. If left untreated, aliasing errors will result in a catastrophic amplification of the high wavenumbers represented by a model grid mesh.

Several methods have been developed to control aliasing errors in FD models. However, each method tends to have undesirable side effects. For example, low-pass filters (Shapiro 1970; Purser 1987) and numerical dissipation can be effective at damping the high spatial frequencies that are due to aliasing errors. But filters and dissipation can produce undesirable effects such as Gibbs' phenomena and unphysical damping of longer wavelengths. Alternatively, quadratic conserving FD methods (Arakawa 1966) can be used to keep the growth of aliasing errors bounded. Unfortunately, though, the dispersion and shape-preserving properties of these schemes tend to be poor. In summary, low-pass filters and certain FD methods can control and bound aliasing errors; however, they cannot completely eliminate these errors, as nonlinear products can still be aliased onto longer wavelengths.

In contrast to using FD methods, aliasing errors can be avoided entirely with spectral transform (ST) methods (Orszag 1970; Machenhauer and Rasmussen

Corresponding author address: Dr. Jerry M. Straka, School of Meteorology, University of Oklahoma–Norman, Energy Center Room 1310, 100 East Boyd Street, Norman, OK 73019.

1972). This is because the time tendencies of high spatial wavenumbers not resolved by the model resolution can be truncated in the time integration process. It has been argued by some that dealiasing does not improve solutions of flows that are well resolved. For example, Chen (1991) shows that dealiasing does not necessarily improve his numerical solutions with the ST method. However, Chen's test was for a case of fairly smooth flow that was well resolved and without sharp or collapsing boundaries. While most two-dimensional fluid problems with sharp boundaries can be adequately resolved using current computational technology, many three-dimensional simulations of complex fluid flows often use only marginal resolution due to computational constraints. Thus, either dealiasing or some form of filtering must be imposed to maintain stable solutions.

A problem with ST methods is that they can be difficult to implement in limited-area models with nonperiodic domains. In addition, global knowledge of all velocities in a model domain is required at each time step to compute the nonlinear advection terms for any particular velocity in physical space. As a result, it has also been very difficult, at least in the past, to efficiently implement ST methods on many of the new massively parallel processing (MPP) computers. Efficient use of these machines generally requires a minimum of interprocessor communication between all but adjacent processors. In more recent years, progress has been made in deriving alternative schemes from classical ST methods that show promise for use on MPP computers. An example of this type of scheme is the spectral element method discussed by Fishcer (1990).

Another alternative to the ST method is the minimal aliasing local spectral (LS) method, developed by Anderson (1989, hereafter referred to as A89). The LS method is a numerical technique, derived from digital-filtering theory, that retains the local nature of FD methods and the minimum aliasing properties of ST methods. The LS method is similar to FD methods in that they both use a limited number of nearby grid points to influence the solution at a particular grid point in the time integration process. In contrast to the FD methods, the LS method uses the general algorithmic structure of the ST methods to avoid aliasing errors by computing the nonlinear tendencies at high resolution and then truncating the unresolvable high-spatial wavenumber time tendencies. Without dealiasing filters, the LS method collapses to a high-order FD scheme. When filter lengths are chosen to span the integration domain and the dealiasing stage is retained, the LS method becomes an ST method. For the interested reader, a complete discussion of the development of the LS method and a documentation of the robustness, accuracy, and minimum aliasing properties of the LS method in integrating the one-dimensional prognostic nonlinear advection–linear diffusion equation on a periodic domain are described by A89. It should be pointed out that there are other types of numerical schemes such as the sum-accelerated pseudo-spectral methods (e.g., Boyd 1991) and the those with various smoothing operators (e.g., Van der Houwen *et al.* 1990), which are similar in some respects to the LS method.

An advantage of the LS method over the FD methods is that the cutoff for the truncation filters used in the LS method is not necessarily as low as the cutoff for the low-pass filters required to keep many FD methods stable. This is because FD methods must use spatial filters that remove spatial frequencies larger than $3\pi/2$ to control the growth of aliasing errors (Orszag 1971). As a result, the effective grid resolution in FD models can be compromised by low-pass filters. Furthermore, nonlinear products that are aliased onto longer wavelengths cannot be completely eliminated in FD models with low-pass filters. An advantage of the LS method over ST methods is that it can be used in limited-area domains with open boundary conditions without difficulty. Furthermore, the local nature of the LS method makes it suitable for use on MPP computers.

more computationally intensive, especially in multidimensions, than standard FD methods. A more computationally efficient version of the LS method is being developed, and hopefully will be described in a future paper. Finally, the LS method suffers from a spectral blocking problem similar to the one that occurs with ST methods. By this we mean that the cascade of energy to the highest wavenumbers can be blocked. But this is usually of minor consequence compared to the advantages of the LS method, which include high accuracy and minimal aliasing error.

For completeness, an overview of the LS method as applied to the one-dimensional case is presented in section 2. The LS method in multidimensions is described in section 3. A two-dimensional nonlinear density-current test problem, which is used to evaluate the performance of the LS model, is discussed in section 4. Results from simulations of the test problem with a very high resolution reference model, an LS model, and a high-order FD model are compared in section 5. Finally, the paper is summarized in section 6. A design for the interpolation, differentiation, and truncation filters required by the LS method based on order-of-accuracy-preserving Lagrange polynomials is presented in appendix A.

2. Review of the local spectral method

In this section we review four distinct steps that are required to implement the LS method in one dimension. As shown in Fig. 1, and described in the following, these four steps include 1) interpolation of the dependent variables from the original model grid to a high-resolution grid, 2) computation of the derivatives of the dependent variables on the high-resolution grid us-

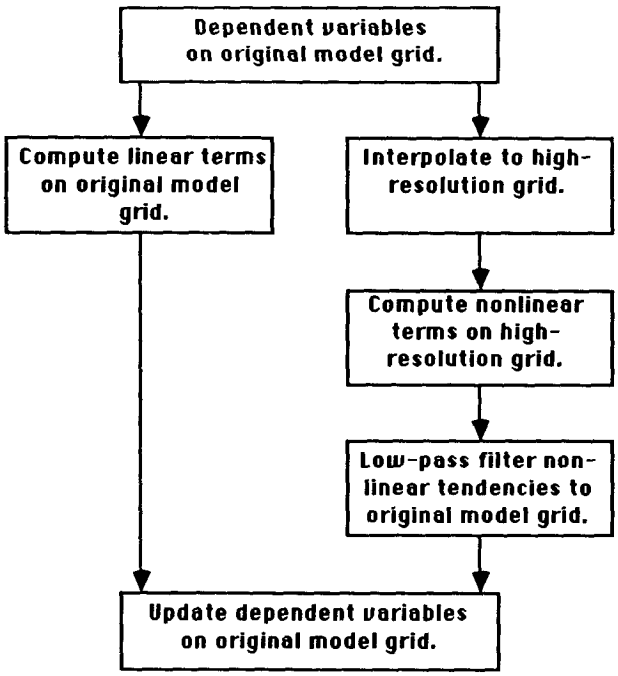

FIG. 1. Flowchart describing the design of local spectral methods in one dimension.

ing the dependent variables on the original model grid, 3) computation of nonlinear tendencies of the dependent variables on the high-resolution grid, and 4) projection of the truncated nonlinear tendencies from the high-resolution grid back to the original model grid.

The LS method is derived from the view of representing each continuous variable $q(x)$ in terms of discrete samples: $q_i = q(i\Delta x)$. The well-known Nyquist sampling theorem can be employed to recover the continuous q from these samples as long as q is strongly band limited (i.e., its spatial spectrum is zero for all wavenumbers above $k = \pi/\Delta x$); that is, it can be represented by,

$$q(x) = \int_{-\pi/\Delta x}^{\pi/\Delta x} Q(w) e^{iwx} dw. \tag{1}$$

When this condition is met, q is recovered using

$$q(x) = \int_{-\infty}^{+\infty} h(x') \sum_i \delta(x - i\Delta x - x') q_i dx' = \sum_i h(x_i - i\Delta x) q_i, \tag{2}$$

where δ is the Dirac delta function and

$$h(x') = \frac{\sin(\pi x' \Delta x^{-1})}{(\pi x' \Delta x^{-1})}. \tag{3}$$

The frequency response of the filter given by $h(x')$ is unity for all wavenumbers below $k = \pi/\Delta x$ and zero for all higher wavenumbers.

If the practical problems with the infinite integral bounds are ignored, (2) provides an exact, continuously differentiable expression for q at any point in the domain, and thus, can form the basis for the computation of any linear or nonlinear term in the differential system that contains no errors in addition to those that are inherent in the original description of q.

Using (2), we can compute samples of the differential forcing terms at any point in x that are needed. It is useful to note that the leading nonlinear terms in fluid flows are generally the quadratic nonlinear terms, which we denote with $r(x)$, and can always be written in the following form if the condition given by (1) holds:

$$r(x) = \int_{-2\pi/\Delta x}^{2\pi/\Delta x} R(w) e^{iwx} dw. \tag{4}$$

In (4), $r(x)$ is given by

$$r(x) = \mathbf{L}[q(x)]\mathbf{M}[q(x)], \tag{5}$$

and $\mathbf{L}$ and $\mathbf{M}$ can be general linear differential operators. The expression for r given by (4) indicates that r is band limited to twice the spatial frequency of q and can be written in terms of samples r_i but this time on a sample grid with one-half the grid interval of the one needed to represent q,

$$r(x) = \int_{-\infty}^{+\infty} h(x') \sum_i \delta\left(x - \frac{i\Delta x}{2} - x'\right) r_i dx' = \sum_i h\left(x - \frac{i\Delta x}{2}\right) r_i, \tag{6}$$

where $r_i = r(i\Delta x/2)$, and

$$h(x') = \frac{\sin(2\pi x' \Delta x^{-1})}{(2\pi x' \Delta x^{-1})}. \tag{7}$$

The problem now comes when we have a representation for $r(x)$ that involves twice as many degrees of freedom as our original representation of $q(x)$, and we need to implement a time-differencing scheme along the lines of

$$q(x, t + \Delta t) = q(x, t) + \Delta t r(x). \tag{8}$$

To prevent the exponential growth of the model state we will need to somehow degrade our representation of r, a process generally known as truncation. The method chosen here is critical to the behavior of a model for nonlinear problems.

One approach is to simply ignore the values of r on the odd points and generate a new continuous r, represented by r' from

$$r' = \int_{-\infty}^{+\infty} h(x') \sum_i \delta(x - i\Delta x - x') r(i\Delta x) dx' = \sum_i h(x - i\Delta x) r(i\Delta x), \tag{9}$$

with

$$h(x') = \frac{\sin(\pi x' \Delta x^{-1})}{(\pi x' \Delta x^{-1})}. \quad (10)$$

Following this approach yields the semispectral method when (9), for example, is evaluated exactly on a periodic domain; various finite-difference methods result when the integral in (9) is truncated in some fashion at finite x'. In each case, the effect of ignoring the odd samples of r is to introduce an aliasing error into the calculation, which can result in the need for increased computational dissipation to control nonlinear instability (e.g., A89).

An alternative approach is to filter r so as to eliminate the spatial frequency components that prevent its representation on the same sample interval as q. The filtering process that eliminates all of these frequencies without affecting any of the resolved frequencies is given by

$$r' = \int_{-\infty}^{+\infty} h(x') r(x - x') dx', \quad (11)$$

with

$$h(x') = \frac{1}{\Delta x} \frac{\sin(\pi x' \Delta x^{-1})}{(\pi x' \Delta x^{-1})}. \quad (12)$$

When this technique is applied on a periodic domain, where (2) and (11) can be computed exactly, we recover the well-known Galerkin spectral technique with discrete sinusoidal basis functions. The local spectral method results from a truncation of (2) and (11) at finite x'. A89 used digital filter techniques (e.g., Oppenheim and Schafer 1975) to generate the truncated version of $h(x')$ based on the window function used in spectral estimation by Papoulis (1973). Ideally, one might choose to use orthogonal polynomials to be consistent with true spectral schemes in multidimensions. In this paper we will consider an alternative approach, namely, one where the interpolation techniques defined by (2) reduce to high-order finite-difference operators. A similar approach is applied to (11) to produce dealiasing filters consistent with the interpolation filters. The aliasing in an LS model can be, for the most part, eliminated by appropriately filtering the nonlinear tendencies. The amount of aliasing leaked in the dealiasing stage is regulated in part by the length of the dealiasing filters. In most practical applications, dealiasing filters that allow a small amount of aliasing are necessarily used. This small amount of aliasing probably would not cause any serious consequences in long-term integrations if some form of the subgrid parameterization for the diffusion terms in the Navier–Stokes equations is used.

Based on results with various polynomial forms, we have found that the best solutions for simple linear and nonlinear problems with the LS method are achieved with Lagrange polynomials. The design for the LS method, based on the use of Lagrange polynomials, is described in appendix A. The algorithmic structure and other necessary information to implement the LS method are also reviewed in appendix A.

3. Local spectral method in multidimensions

To extend the LS method to more than one dimension, there are three issues that need to be resolved: 1) the form of the high-resolution grid, 2) the implementation of the interpolation stage, and 3) the implementation of the dealiasing stage.

If we continue to require that the LS scheme provide asymptotically nonaliased results in the limit of long filter lengths, the choice of the nonlinear grid is fixed in the same way as for spectral transform models. The condition requires that the high-resolution grid be a fully filled grid with a spacing no larger than $\frac{2}{3}\Delta x$ in the x direction, $\frac{2}{3}\Delta y$ in the y direction, and $\frac{2}{3}\Delta z$ in the z direction. The factor of $\frac{2}{3}$ in the grid spacing is due to the allowable relaxation from strict fine-grid representation described by Orszag (1971). As in the one-dimensional case, we will choose a fine-grid spacing of $\frac{1}{2}\Delta$ for the convenience of having collocation of every other fine-grid point with an original grid point. For multiple dimensions, this trade-off is not quite as clear since a three-dimensional $\frac{1}{2}\Delta$ grid contains 8.0 times as many points as the original grid, while a $\frac{2}{3}\Delta$ grid contains only approximately 3.4 times as many points.

At this point we should also note that the fully filled nonlinear grid can be avoided by the use of the forward-in-time "dimension splitting" techniques (e.g., Tremback et al. 1987). For these types of schemes, the dealiasing is performed only along the advection direction, eliminating the shocklike aliasing terms. These techniques can offer very good performance and significant cost reductions; however, they do have aliasing errors, which result from ignoring the cross-space terms. The results for this kind of approach will be presented in a future paper.

The interpolation step for multidimensional problems is straightforward and is simply the application of (2) and (3) in multiple one-dimensional passes. Specifically, $q(x_0, y_0, z_0)$ is computed, for example, by first interpolating a two-dimensional discrete x, y grid to $z = z_0$. This result is then interpolated to a one-dimensional x grid at $y = y_0$, $z = z_0$. Finally, $q(x_0, y_0, z_0)$ is found as before.

The extension of the dealiasing step is somewhat more complicated since it involves some decisions that must be made about the form of the model truncation. The most straightforward and computationally efficient approach is to perform the dealiasing stage one dimension at a time in a fashion analogous to the interpolation stage:

$$r' = \int_{-\infty}^{+\infty} h_x(x') \int_{-\infty}^{+\infty} h_y(y') \int_{-\infty}^{+\infty} h_z(z') r \times (x - x', y - y', z - z') dz' dy' dx'. \quad (13)$$

This approach yields a solution that is asymptotically nonaliased. The dealiasing is accomplished by truncating the results at specific wavenumbers in each dimension. The process is analogous to the use of rhomboidal truncation in spectral models, and shares many properties of that truncation, including a lack of invariance to the rotation of the coordinate system.

If rotational invariance is required, then the truncation step must be performed using a full three-dimensional convolution sum involving a three-dimensional filter kernel that performs the solution truncation on terms of total wavenumber rather than component wavenumbers. This choice is analogous to the use of triangular truncations in spectral models.

In this paper we have chosen to use the noninvariant form (13), because of the computational efficiency of its discrete implementation. One should keep in mind that there may be applications, particularly those involving polar or spherical coordinates, where the extra expense of the invariant form may be worthwhile.

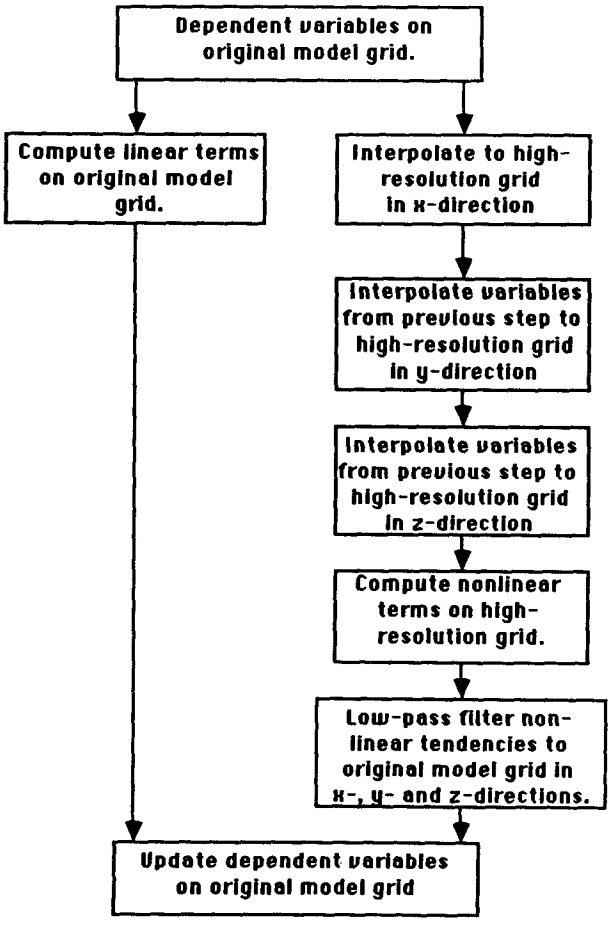

FIG. 2. Flowchart describing the design of local spectral methods for multidimension applications.

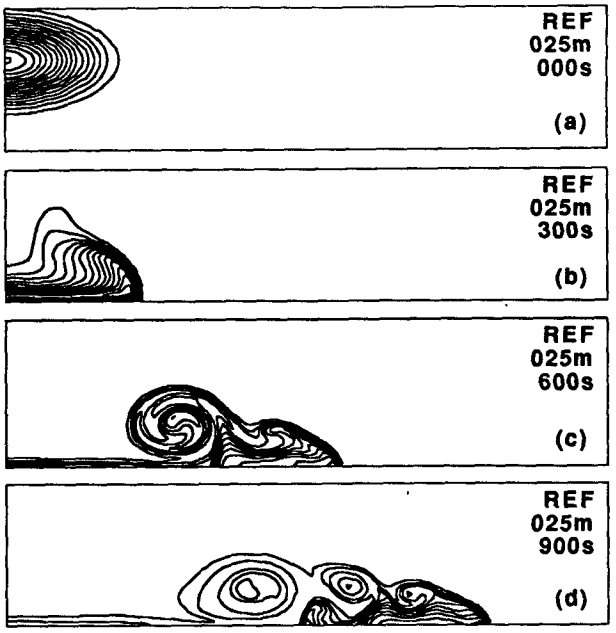

FIG. 3. Plots of θ' at (a) 0 s, (b) 300 s, (c) 600 s, and (d) 900 s for the 25.0-m resolution compressible reference model solution. The contour interval (CI) is 1°C, and the contours are centered around 0°C. The minimum value of θ' at 0 s is −16.624°C. Note that only the lower-left three-quarters of the domain is shown.

A block diagram of the computational architecture for the LS method on a multidimensional grid is presented in Fig. 2. The four steps required to implement the LS method in multidimensions are similar to those for the one-dimensional case, except for modifications to accommodate multidimensions.

4. Meteorological test problem

To test the performance of the LS method in multidimensions, we made simulations of a diffusion-limited two-dimensional nonlinear density-current test problem. The evolution of the density current from a high-resolution 25.0-m reference simulation is shown in Figs. 3 and 4. The density current was initiated as a cold blob of air that subsequently descended to the ground. As the density current spread out laterally at the lower boundary, Kelvin–Helmholtz shear instability rotors formed along the top of the cold-air boundary. With the finescale structures in the Kelvin–Helmholtz rotors and the strong nonlinearities in the flow fields, the foregoing test problem serves as a challenge for testing numerical techniques, as was demonstrated at a recent workshop on numerical methods (Straka et al. 1991; and Straka et al. 1993).

The system of governing equations for the density current test problem is written in the computationally efficient quasi-compressible form (Anderson et al.

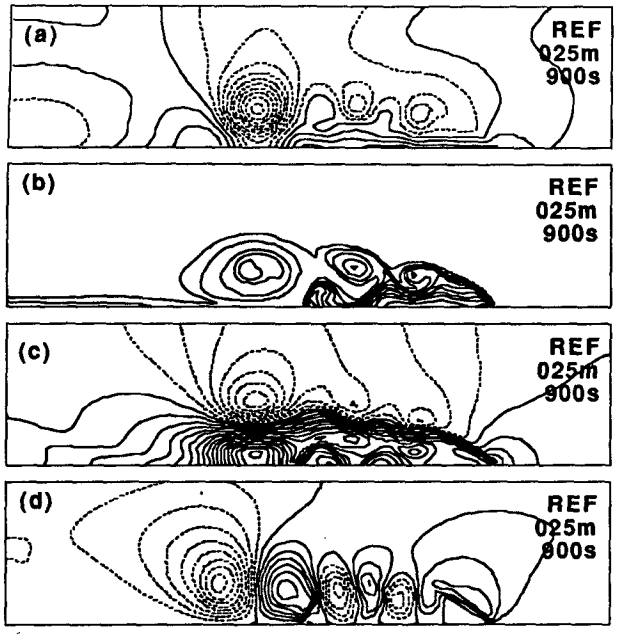

FIG. 4. Figure of (a) p' (contour interval of 50 Pa), (b) θ' (contour interval of 1°C), (c) u (contour interval of 2 m s^{-1}), and (d) w (contour interval of 2 m s^{-1}) at 900 s from the REF model using 25.0-m resolution. All contours are centered around a zero contour. Note that only the lower-left three-quarters of the domain is shown.

1986; Droegemeier and Wilhelmson 1987), and includes equations for pressure (14), horizontal velocity (15), vertical velocity (16), and potential temperature (17):

$$p'_t = -c_s^2[(\bar{\rho}u)_x + (\bar{\rho}w)_z] \tag{14}$$

$$u_t + uu_x + wu_z + \frac{1}{\bar{\rho}}p'_x - K_d(u_{xx} + u_{zz}) = 0 \tag{15}$$

$$w_t + uw_x + ww_z + \frac{1}{\bar{\rho}}p'_z + g\left(\frac{\theta'}{\bar{\theta}} - \gamma\frac{p'}{\bar{p}}\right) - K_d(w_{xx} + w_{zz}) = 0 \tag{16}$$

$$\theta'_t + u\theta'_x + w\theta'_z - K_d(\theta'_{xx} + \theta'_{zz}) = 0. \tag{17}$$

The equation of state and the Exner function are given by (18) and (19), respectively:

$$p = \rho R_d T \tag{18}$$

$$\pi = (pp_0^{-1})^{\kappa}. \tag{19}$$

In (14)–(19), u is horizontal velocity, w is vertical velocity, ρ is density, p is pressure, and θ is potential temperature. Variables with an overbar are base-state variables that are a function of z, and primed variables are perturbations from the base state. For example, θ' is given as $\theta' = (\theta - \bar{\theta})$. The independent variables x, z, and t are the horizontal and vertical Cartesian grid directions, and the time, respectively. Variables and quantities subscripted with t, x, and z are derivatives with respect to these independent variables. Note that SI (Système International) units are used throughout the model. Other constants include $\kappa = R_d C_p^{-1}$; $T = \pi\theta$ (temperature); $R_d = 287.0$ J kg^{-1} K^{-1} (gas constant for dry air); $C_p = 1004.0$ J kg^{-1} K^{-1} (specific heat at constant pressure); $C_v = 717.0$ J kg^{-1} K^{-1} (specific heat at constant volume); $p_0 = 100\,000.0$ kg m^{-1} s^{-2} (reference pressure); $g = 9.81$ m s^{-2} (gravitational parameter); $K_d = 75.0$ m^2 s^{-1} (diffusion coefficient); and $\gamma = C_v/C_p$ and $T_s = \theta = 300.0$ K (surface temperature). Finally, temperature is defined as $T = \pi\theta$. The quasi-compressible pressure is computed with a pseudo-sound speed of $c_s = 150.0$ m s^{-1} to save computational costs. Anderson et al. (1986) and Droegemeier and Wilhelmson (1987) have shown that the quasi-compressible system is accurate when c_s is greater than twice the fastest wave mode in the system. In addition, Anderson et al. (1986) and Chorin (1967) have shown that the quasi-compressible system approaches the anelastic system in the limit as $c_s \to \infty$.

The free-slip condition on the velocity components is imposed at the walls of the domain. The lateral boundary conditions for the test problem are $u = w_x = p_x = \theta_x = 0$, and the vertical boundary conditions are $w = u_z = p_z = \theta_z = 0$. For real atmospheric problems, the vertical pressure gradient at the upper and lower boundaries would typically follow from the vertical equation of motion with $w = 0$ at the vertical boundaries. To simplify the test problem, a reflective condition is applied to p at the upper and lower boundaries.

The base-state variables are defined as a function of z by the following:

$$\bar{T} = T_s - zgC_p^{-1}, \quad \bar{p} = p_0(\bar{T}T_s^{-1})^{\kappa}$$

$$\bar{\rho} = \bar{p}(R_d\bar{T})^{-1}, \quad \frac{d\bar{p}}{dz} = -\bar{\rho}g$$

$$\bar{\theta} = T_s = 300 \text{ K}, \quad u = v = 0.0. \tag{20}$$

To provide the negative buoyancy necessary to initiate a density current, the following function is used to specify a temperature perturbation:

$$\Delta T = \begin{cases} 0.0°\text{C}, & L > 1.0 \\ -15.0°\text{C}\,[\cos(\pi L) + 1.0]/2, & L \leqslant 1.0, \end{cases} \tag{21}$$

where $L = \{[(x - x_c)x_r^{-1}]^2 + [(z - z_c)z_r^{-1}]^2\}^{0.5}$, $x_c = 0.0$ km, $x_r = 4.0$ km, $z_c = 3.0$ km, and $z_r = 2.0$ km. The quantity $\Delta\theta$ can be evaluated from ΔT and the relation $T = \theta\pi$. The minimum temperature in the thermal perturbation is −15.0°C, and it is centered at $x = 0.0$ km, which is in the middle of the domain. With the initial and boundary conditions described earlier, the domain is symmetric about the vertical line

at $x = 0.0$ km, and is periodic over the interval from -25.6 to 25.6 km. To minimize computational costs, the symmetry of the problem is exploited. A plot of the initial θ' temperature field is shown in Fig. 3a, with the thermal perturbation centered on the symmetric left boundary ($x = 0$).

5. Results and discussions

a. Reference solutions of the test problem

To standardize the comparisons of the solutions of the test problem, we made a set of simulations with a quasi-compressible reference model. This model (hereafter called the REF model) was integrated using standard second-order centered-in-time and centered-in-space differences on an unstaggered grid (Arakawa A grid, Arakawa and Lamb 1977). A time filter was used to prevent separation of solutions that can occur with centered time differences (Asselin 1972). The form of this filter is $\phi^{t^*} = (1 - 2\alpha)\phi^t + \alpha(\phi^{t-\Delta t} + \phi^{t+\Delta t})$, where ϕ is any prognostic variable and $\alpha = 0.10$ is the filter coefficient. The advection terms were differenced using a second-order quadratic conserving scheme (Matsuno 1966; Kurihara and Holloway 1967). To maintain linear stability, the diffusion terms were integrated from time $t - \Delta t$ with a forward-in-time differencing scheme. The reference simulations were initiated with a thermal perturbation as described already, and integrated to 900 s. A converged solution (hereafter called the REF solution) was obtained with a grid resolution of 25.0 m. A complete discussion of the evolution of the simulated density current test problem is described in Straka et al. (1991) and Straka et al. (1993); thus, only a brief discussion of the grid-converged REF solution and how it was obtained is presented in the following.

The evolution of the θ' fields in the REF solution is shown in Fig. 3. In addition, the p', θ', u, and w fields at 900 s from the REF solution are shown in Fig. 4. During the first 300 s of the simulation, the initial negatively buoyant thermal descended toward the lower boundary. As pressure at the lower boundary increased beneath the descending downdraft, a strong horizontal outflow of cold air developed in the lowest levels. Kelvin–Helmholtz shear instability then formed along the top and front of the outflow, and resulted in the formation of at least three rotors. The first rotor was well developed by 300 s, the second by 600 s, and the third by 900 s. The older rotors were left behind in the wake of the current's leading edge as the new rotors formed at the front. There is a hint at 900 s of a perturbation on the front, which will grow into the fourth rotor. The aforementioned evolution is typical of density current development in a constant potential temperature environment with no vertical wind shear (Droegemeier and Wilhelmson 1986).

The 25.0-m resolution for the reference solution was determined by successively halving the grid resolution in simulations, starting from 400.0-m resolution, until no significant improvement in the solutions could be achieved. To visually demonstrate the convergence of the REF solutions, θ' solutions at 900 s made with resolutions of 25.0, 50.0, 100.0, and 200.0 m are shown in Fig. 5. With 200.0-m resolution, the REF model solutions are in significant error. At a resolution of 100.0 m, most of the flow features are well resolved; however, there are significant differences when compared to the 25.0-m solution. For example, there are significant phase speed errors with the locations of the front and the three rotors. As the resolution is reduced to less than 100.0 m, the θ' solutions quickly converge. This is clearly seen in a visual comparison of the 25.0- and 50.0-m solutions. Based on Fig. 5, the basic flow features of the test problem can be considered to be adequately resolved with 100.0-m resolution, and marginally resolved using 200.0 m. Thus, the remainder of this study will focus on the solutions made with resolutions of 100.0 and 200.0 m.

An "extrapolation" method (Conte and de Boor 1980) was also used to determine if the solutions were spatially and temporally converged. These results, which are described in Straka et al. (1993), show that there would be little if any improvement in the solutions at higher spatial or temporal resolutions. For example, the maximum absolute errors in the θ', u, w, and p' fields in the REF solution, as compared to the extrapolated solution (computed from the 25.0- and 50.0-m REF model solutions), are on the order of 10^{-4}

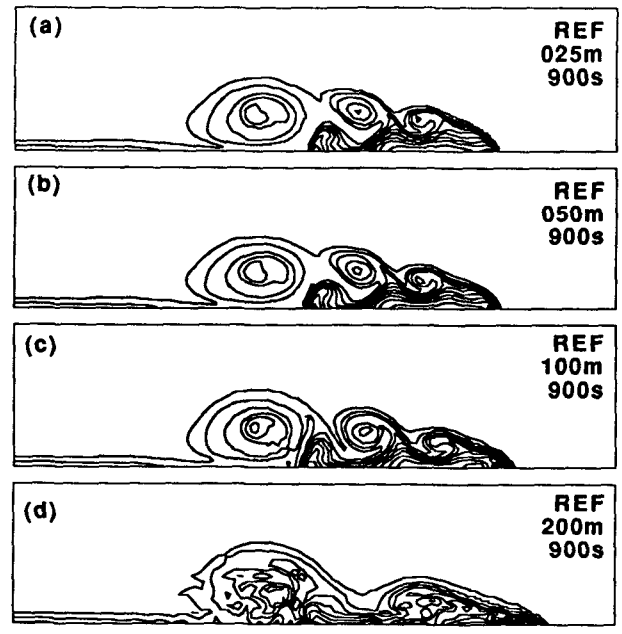

FIG. 5. Figure of θ' solutions at 900 s (contour interval of 1°C) for the (a) 25.0-m, (b) 50.0-m, (c) 100.0-m, and (d) 200.0-m resolution REF model solutions. All contours are centered around a zero contour. Note that only the lower-left three-quarters of the domain is shown.

in space and 10^{-3} in time. With these results we have concluded that the 25.0-m reference solution is converged, at least for the purposes of this paper. At resolutions of 33.3 (not shown) and 50.0 m, there are only minimal errors in the solutions.

The convergence behavior of the REF model solutions is evaluated quantitatively by computing the L_2 norm (22) of the θ' solutions as

$$L_2(\theta') = \left\{ \frac{1}{(\mathrm{NX})(\mathrm{NZ})} \sum_{i=1}^{\mathrm{NX}} \sum_{k=1}^{\mathrm{NZ}} [\theta'(x_i, z_k) - \theta'_{\mathrm{ref}}(x_{ii}, z_{kk})]^2 \right\}^{0.5}, \quad (22)$$

where NX and NZ are the number of grid points in the x and z directions in any particular solution, i and k are the grid indices in this solution, and ii and kk are the grid locations in the REF solution that correspond to i and k. The $\theta' L_2$ norms for solutions from the REF model for various resolutions between 33.3 and 533.3 m are shown in (Fig. 6). The lines in Fig. 6 labeled with $O(1)$ and $O(2)$ represent first-order and second-order spatial convergence. Using the REF solution as the true solution, the REF model produces, not unexpectedly, second-order convergence at resolutions that are better than 133.3 m.

b. *Local spectral solutions*

In this section, we describe results of the test problem using an LS model. First, the basic numerical techniques used in the LS model are described. The time integration and computation of diffusion terms in the LS model are done as they are in the REF model. The order of an LS model is limited primarily by the length and order of accuracy of the interpolation, differentiation, and truncation filters. In general, an LS model with a filter length of $2R$ can be considered to be analogous to an N-order FD model (e.g., $2R = N$, A89). All first-order derivatives in the LS model are approximated with $2R$-order LS approximations for models described as being $2R$ order. The time steps for $2R$-order LS models are based on the linear stability for N-order FD models, as described in appendix B.

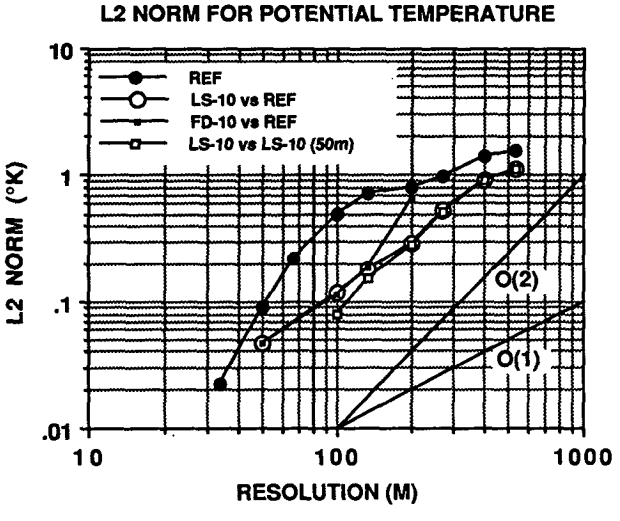

FIG. 6. The L_2 norms for θ' computed against the 25.0-m resolution reference solution from the REF model for the REF model, the 10th-order LS model, and the 10th-order FD model. Also shown is a self-convergence test of the 10th-order LS solutions against the 50.0-m 10th-order LS solution. Lines labeled with $O(1)$ and $O(2)$ represent first-order and second-order spatial convergence.

The θ' solutions at 900 s from 2d-, 6th-, and 10th-order LS models with 100.0- and 200.0-m resolutions are shown in Fig. 7. (Tests with models with up to 20th-order LS representations show very little additional improvement compared to 10th-order representations.) In addition, the p', θ', u, and w solutions from the 10th-order LS model with 200.0-m resolution are shown in Fig. 8. The values of maximum and minimum θ' in these solutions are shown in Table 1. Not unexpectedly, the 100.0-m LS model solutions capture all of the basic features of the flow extremely well, especially the solutions made with the 6th- and 10th-order schemes. Similarly, the 10th-order 200.0-m LS model solutions also contain all of the basic features of the flow. The small-amplitude two-delta noise in the 200.0-m solutions made with the LS model is similar to "spectral blocking" in underdiffused solutions made with ST models (A89).

In comparison, the low-resolution REF model solutions (e.g., 200.0 and 100.0 m) are significantly worse than those made with the LS model with equivalent resolutions. It appears that solutions can be made with the LS model—using two to three times less resolution—that are as accurate as those made using the REF model. For example, the 100.0-m 10th-order LS model solution appears to be as good as the REF solution and better than the 50.0-m REF model solutions. In addition, the 200.0-m 10th-order LS model solution has essentially the same phase speed errors as the 50.0-m REF model solution.

The L_2 norms of the θ' solutions from the LS simulations, based on comparisons with the REF solution, as well as a comparison to a 50.0-m-resolution LS model solution (to test self-convergence) are shown in Fig. 6. From Fig. 6, it can be seen that the L_2 norms for the LS model solutions are up to five times smaller than those from the REF solutions for the same resolution. (The L_2 norms for p', u, w, and vorticity are behave similarly to those for θ'.) In addition, the L_2 norms from the self-convergence test of the LS model solutions show better convergence at coarse resolution than the REF model.

To further evaluate the LS model solutions, the dissipation, dispersion, and total errors (Takacs 1986) were computed using the REF solution as the truth solution (Table 1). (The total error is the sum of the dissipation error and the dispersion error.) As is clearly

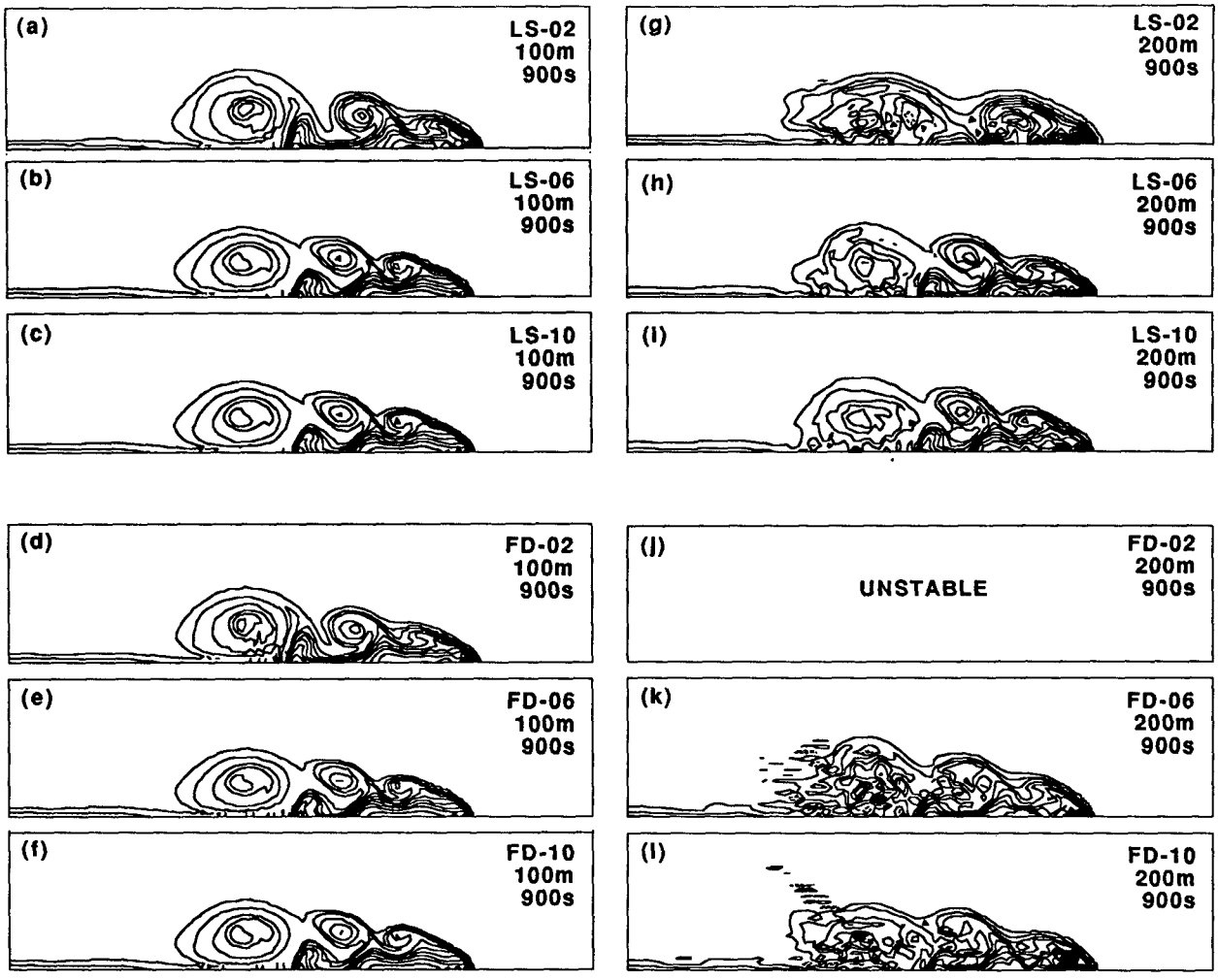

FIG. 7. Solutions of θ' (contour interval of 1°C) at 900 s made with the 2d-, 6th-, and 10th-order LS models and FD models using resolutions of 100.0 and 200.0 m. All contours are centered around a zero contour. Note that only the lower-left three-quarters of the domain is shown.

seen in Table 1, the primary errors in the LS model solutions, and also in the other solutions, are due to dispersion (phase speed) errors. In addition, the dispersion errors are several orders of magnitude larger than the dissipation errors, which are greatest for the low-order simulations.

The location of the front of the density current at 900 s is also used to measure the phase speed characteristics of the different models. As can be seen in Fig. 9, the location of the front in the 200.0-m 10th-order LS model solution is about as accurate as that for the 50.0-m REF model solution. The low-order LS model solutions also accurately simulate the front location, even at coarser resolutions (Fig. 7).

For further comparison, simulations of the test problem were made with an FD model. This model was integrated using standard 2d-, 6th-, and 10th-order FD approximations (Purser and Leslie 1988). Note that the FD model is different from the REF model in that the REF model uses a second-order quadratic conserving scheme. The θ' solutions from the FD model simulations, with resolutions of 100.0 and 200.0 m, are shown in Fig. 7. In addition, the wind and pressure solutions for the 200.0-m 10th-order FD model are shown in Fig. 8. The convergence behavior and error statistics of the 10th-order FD model are shown in Fig. 6 and Table 1, respectively. Not unexpectedly, the 100.0-m FD model solutions are nearly identical to the high-order 100.0-m LS model solutions. At this resolution, all of the flow features are adequately resolved. Using 200.0-m resolution, there are noticeable differences between the FD and LS model solutions. For example, the 6th- and 10th-order FD model solutions are very noisy, and are contaminated with aliasing errors. The second-order FD model solution is not shown, because it became unstable well before 900 s. It should be noted that the higher-order FD solutions also became unstable shortly after 900 s. In addition,

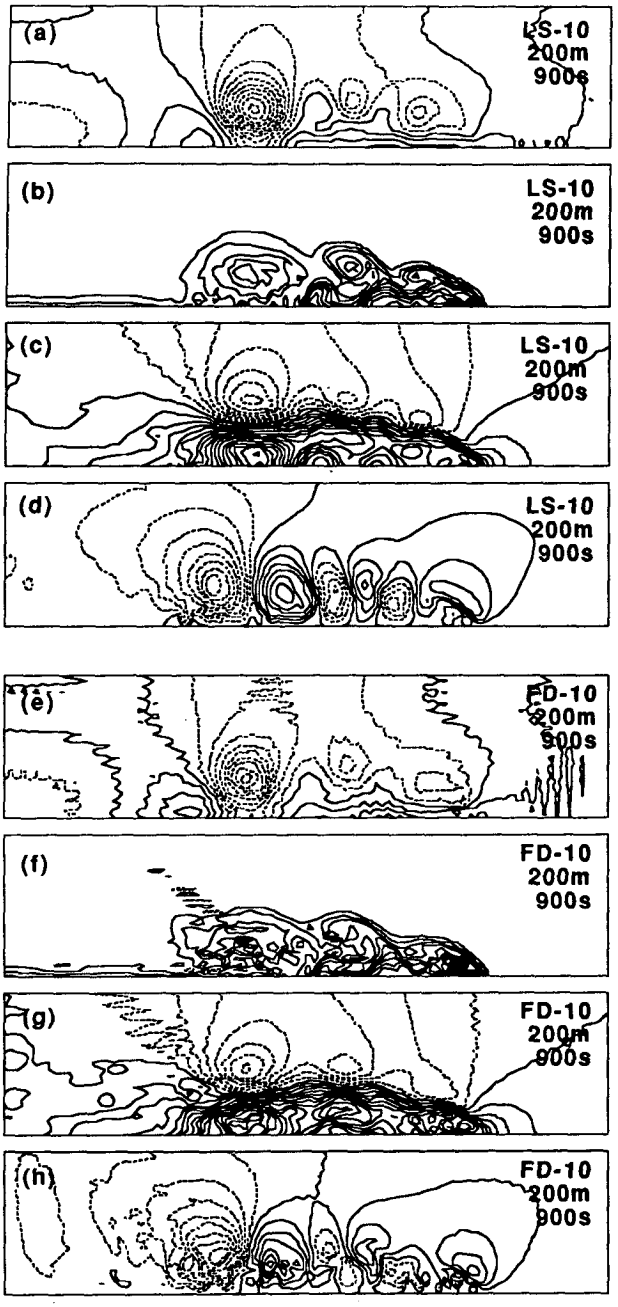

FIG. 8. Figure of [(a) and (e)] p' (contour interval of 50 Pa), [(b) and (f)] θ' (contour interval of 1°C), [(c) and (g)] u (contour interval of 2 m s^{-1}), and [(d) and (h)] w (contour interval of 2 m s^{-1}) at 900 s from a 10th-order LS model and a 10th-order FD model using a resolution of 200.0 m. All contours are centered around a zero contour. Note that only the lower-left three-quarters of the domain is shown.

the FD model quickly became unstable with resolutions larger than 200.0 m. In contrast, the LS model solutions were stable in simulations that were carried out to 1200 s and beyond, with resolutions as large as 533.33 m.

As suggested by Purser (1987) and others, various spatial filters can be applied to control the growth of the high-frequency spatial perturbations that occur in high-order FD models. These filters can be applied every time step or every few time steps. In addition, they can be applied with the maximum stable Courant number (maximum smoothing using a particular form of a filter) or with a relaxed Courant number (reduced smoothing from a filter). The MASS (mesoscale atmospheric simulation system) model described by Kaplan et al. (1982), for example, uses filters applied with the maximum stable Courant number. In contrast, the Klemp and Wilhelmson (1978) model, for example, uses filters applied with a relaxed Courant number. Since the dealiasing is done in our LS models using filters applied every time step with the maximum stable Courant number, the same is done with filters in our FD models. When the features of the flow are well resolved, such as when 100.0-m resolution is used with the test problem, the impact of a 10th-degree filter [$R = 5$, $S = 0$: Purser (1987), and appendix A] on solutions made with a 10th-order FD model is minimal. However, a degradation of the solutions can occur with the use of filters when the resolution is marginal, as was observed in the θ' solutions from a 200.0-m resolution simulation made with the same 10th-order FD model and 10th-degree filter (not shown; however, see FD-10FILT-200.0-m error statistics in Table 1). Basically, these solutions appeared to be overdamped. In contrast, the 200.0-m LS solutions actually improved (LS-10LC-200.0-m error statistics in Table 1) using a more dissipative dealiasing filter than the dealiasing filter used to make the solutions shown in Fig. 7. Note that the dealiasing filter used in the modified LS model actually damped higher-frequency spatial waves more than the filter used in the FD model. Finally, we point out that FD model solutions can be produced with 200.0 m that are comparable to those made using the LS model by using filters within the FD model that are applied with a reduced Courant number.

It was noted in the Introduction that the only situations in which dealiasing helps improve a numerical solution in spectral-type models is when the flows are marginally resolved. Yet, in modeling complex fluid flows, the spatial resolution is often marginal or barely adequate due to computational constraints, especially in three dimensions. This seems particularly true for simulations of flows with sharp or collapsing boundaries.

For highly resolved flows, we have found that dealiasing does not necessarily improve the results from the LS model, at least for short-term integrations such as those shown in this paper. As an LS model without dealiasing is essentially identical to a similar-order FD model, solutions from the two would be similar. It is important to note that all FD schemes are aliased. (Local spectral methods are also very slightly aliased due to polynomial interpolations.) Without some form of

TABLE 1. Comparison of θ' maximum, minimum L_2 norm, total error (TOTAL), dispersion error (DISP), dissipation error (DISS), and correlation (CORR). The scheme, order, and resolution information for each comparison are contained in the scheme column. All error calculations were computed against the 25.0-m resolution REF solution. The units for maximums, minimums, and errors are in degrees Celsius. Note that the integration of the second-order FD model was unstable using 200.0-m resolution.

Scheme-order-resolution	θ'_{max}	θ'_{min}	θ' L_2	θ' TOTAL	θ' DISP	θ' DISS	θ' CORR
REF-02-025.0 m	0.0	−10.00					
REF-02-100.0 m	1.34	−15.68	5.04×10^{-1}	2.54×10^{-1}	2.53×10^{-1}	6.95×10^{-4}	9.15×10^{-1}
REF-02-200.0 m	6.12×10^{-1}	−11.67	7.99×10^{-1}	6.34×10^{-1}	6.34×10^{-1}	3.34×10^{-3}	7.94×10^{-1}
LS-02-100.0 m	3.45×10^{-1}	−17.25	5.24×10^{-1}	2.76×10^{-1}	2.74×10^{-1}	1.50×10^{-3}	9.07×10^{-1}
LS-06-100.0 m	6.92×10^{-2}	−11.25	1.20×10^{-1}	1.43×10^{-2}	1.43×10^{-2}	4.47×10^{-6}	9.95×10^{-1}
LS-10-100.0 m	1.02×10^{-1}	−10.41	1.17×10^{-1}	1.38×10^{-2}	1.38×10^{-2}	7.46×10^{-6}	9.95×10^{-1}
LS-02-200.0 m	1.37	−19.94	6.84×10^{-1}	4.68×10^{-1}	4.66×10^{-1}	2.28×10^{-3}	8.50×10^{-1}
LS-06-200.0 m	1.05	−13.23	3.60×10^{-1}	1.28×10^{-1}	1.28×10^{-1}	3.62×10^{-6}	9.60×10^{-1}
LS-10-200.0 m	9.47×10^{-1}	−14.06	2.95×10^{-1}	8.73×10^{-2}	8.72×10^{-2}	1.05×10^{-4}	9.73×10^{-1}
LS-10LC-200.0 m	5.68×10^{-1}	−12.34	2.52×10^{-1}	6.36×10^{-2}	6.36×10^{-2}	2.01×10^{-5}	9.80×10^{-1}
FD-02-100.0 m	6.11×10^{-1}	−17.20	3.84×10^{-1}	1.15×10^{-1}	1.15×10^{-1}	2.23×10^{-4}	9.51×10^{-1}
FD-06-100.0 m	4.22×10^{-2}	−11.59	1.13×10^{-1}	1.27×10^{-2}	1.27×10^{-2}	7.64×10^{-6}	9.96×10^{-1}
FD-10-100.0 m	6.15×10^{-2}	−10.58	1.15×10^{-1}	1.31×10^{-2}	1.31×10^{-2}	1.24×10^{-5}	9.96×10^{-1}
FD-02-200.0 m	unstable	unstable	unstable	unstable	unstable	unstable	unstable
FD-06-200.0 m	1.38	−21.70	5.77×10^{-1}	3.33×10^{-1}	3.33×10^{-1}	3.24×10^{-4}	8.98×10^{-1}
FD-10-200.0 m	1.16	−21.58	6.40×10^{-1}	4.10×10^{-1}	4.02×10^{-1}	7.14×10^{-3}	8.83×10^{-1}
FD-10FILT-200.0 m	1.99×10^{-1}	−15.35	3.40×10^{-1}	1.16×10^{-1}	1.16×10^{-1}	1.56×10^{-7}	9.64×10^{-1}

imposed or inherent filtering or diffusion, solutions from FD methods could eventually become unstable for nonlinear problems.

The importance of applying the dealiasing filters following (13) is highlighted by the following example. If the dealiasing filters are applied only to the x-advection tendencies in only the x direction, y-advection tendencies in only the y direction, and so on [we have called this approach *line local spectral* (LLS)], for example, the solutions are not as good as those with the dealiasing filters applied using (13). This can be seen in Fig. 10, which shows the 900-s θ' solutions made with 10th-order LLS, LS, and FD models using 200.0-m resolution. Notice, though, that the LLS model solutions appear better than those made with similar-order FD models, especially when the flow is marginally resolved.

Next we discuss lateral and vertical boundary conditions, which are often one of the more difficult issues to contend with in nonperiodic limited-area models that use high-order schemes. It has been suggested that

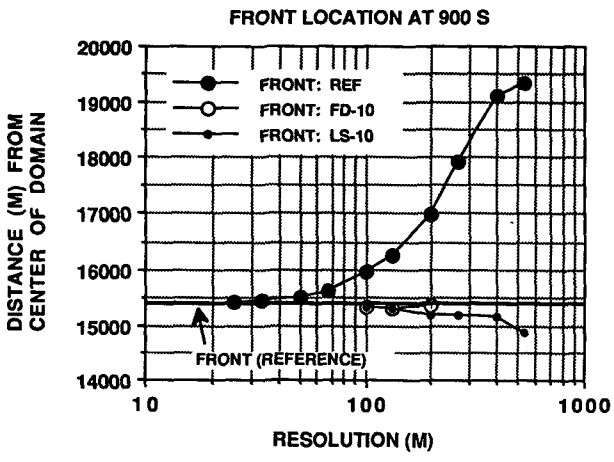

FIG. 9. Location of density-current front, from the left boundary, at 900 s for $z = 0.0$ from the REF, 10th-order LS, and 10th-order FD models using various resolutions from 25.0 to 533.33 m.

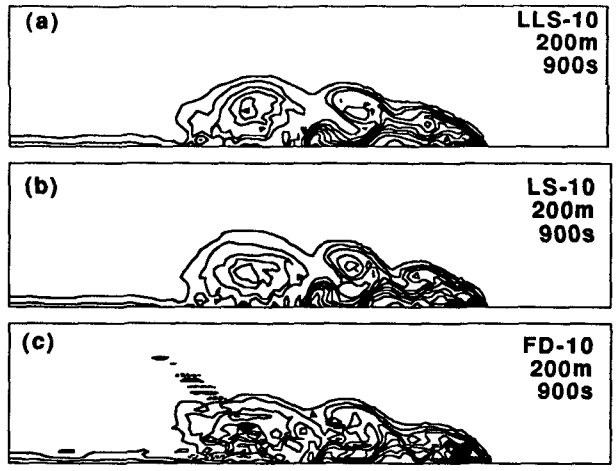

FIG. 10. Solutions of θ' (contour interval of 1°C) at 900 s made with the 10th-order LLS model using 200.0-m resolution and dealiasing only the x direction for x-direction advection, and z direction for z-direction advection. The 200.0-m LS and FD solutions are also shown for comparison. All contours are centered around a zero contour. Note that only the lower-left three-quarters of the domain is shown.

lower-order approximations be used as boundaries are approached (e.g., Klemp and Wilhelmson 1978; Kaplan et al. 1982). At the actual lateral boundaries, some form of upstream differencing (Klemp and Wilhelmson 1978) or extrapolation (Clark 1979) can be used. Following the Klemp and Wilhelmson approach, we use upstream differencing for all variables on the normal boundaries for outflow conditions. For inflow conditions, the normal advection is set to zero. The condition for the normal velocity component is

$$\frac{\partial u}{\partial t} = -(u + c_g)\frac{\partial u}{\partial x},$$

where c_g is the dominant wave speed in the solution. If $u + c_g$ results in inflow, $\partial u/\partial t$ is set to zero. Typically, c_g is set to the dominant internal gravity-wave speed expected in a simulation. For example, Klemp and Wilhelmson use $c_g = 30$ m s^{-1} for simulations of atmospheres that might support deep tropospheric convection.

We have carried out simulations of the test problem with the 10th-order LS model using the boundary conditions just described to demonstrate their feasibility. When the previously described domain size was used, the solutions were essentially identical to those using the idealized boundary conditions described in section 4. We have also carried out simulations using a smaller horizontal domain size ($L_x = 14.4$ km), so that the front rotor of the density current passes through the right boundary. These simulations were made to more stringently test the boundary conditions proposed for the LS method. In making these simulations, we used $c_g = 30$ m s^{-1}; no sensitivity was noted for values of $c_g = 0.0$ m s^{-1} and $c_g = 15$ m s^{-1}. Results of the θ' and u fields from this test using the LS model with 100.0-m resolution are shown in Fig. 11. (Note that the results in Fig. 11 are for the lower-left half of the domain.) The REF and 100.0-m LS model solutions described previously are also shown in the same windowed domain for comparison (Fig. 11). It is evident that the use of lower-order approximations—as the lateral and vertical boundaries are approached—and an outflow condition—at the lateral boundary—do not compromise or significantly influence any part of the solution. In fact, the solutions are very similar. The 200.0-m solutions also behave similarly in that they are not significantly influenced by the aforementioned open boundary conditions.

Finally, a summary of the CPU time required to make the 200.0-m LS and FD model solutions, relative to the 200.0 m REF model solutions, is shown in Table 2. Notice that simulations made with the REF and FD models are less intensive than those made with the LS model. However, as was shown, the LS model provides solutions with up to two to three times the accuracy of the REF model solutions for equivalent resolutions. This means that the LS method can be cost effective against the REF model when flows are marginally resolved. The high-order FD methods produce accurate solutions at higher resolutions for a low cost; however, these solutions are unavoidably aliased. At coarser resolutions, the FD solutions are not as good as the LS solutions unless filters are applied. With higher-order filtering, the cost of using the aforementioned FD methods increases by about 40%–50% for our simple simulations.

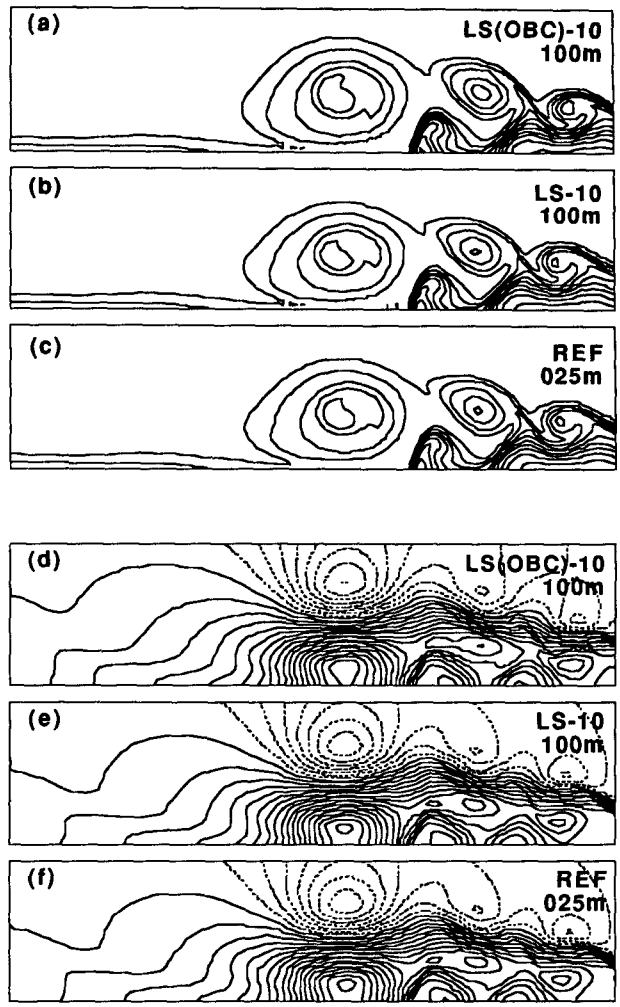

FIG. 11. Solutions of θ' (contour interval of 1°C) and u (contour interval of 2 m s^{-1}) at 900 s made with the 10th-order LS model using 100.0-m resolution in a domain with a horizontal length of 14.4 km and open lateral boundaries. The 100.0-m LS and 25.0-m REF solutions are also shown in the same domain for comparison. All contours are centered around a zero contour. Only the lower-left half of the domain is shown.

6. Summary

In the first part of this paper, the LS method was reviewed from a more rigorous view, and then extended to multidimensions. In the second part of this paper, simulations of a two-dimensional nonlinear density current made using an LS model and various FD models were compared and discussed. These results suggest

TABLE 2. CPU requirements relative to the second-order reference model (REF model).

Model–order	CPU factor
LS-10	5.05
LS-06	2.41
LS-02	1.60
FD FILT-10	2.25
FD FILT-06	1.74
FD FILT-02	1.33
FD-10	1.52
FD-06	1.13
FD-02	1.00

that the LS method was more accurate than similar-order FD methods at coarser grid resolutions, and as accurate as at finer grid resolutions. Furthermore, the LS solutions appeared to be more robust than the FD solutions, especially at grid resolutions that marginally resolve flow features. It was also shown that the LS method can be used with open boundary conditions and lower-order LS "elements" as boundaries are approached. As has been suggested by others, dealiasing techniques appear to improve solutions only when flow fields are marginally resolved. However, many three-dimensional simulations of complex fluid flows often have only marginal resolution due to computational constraints.

At the present time, the potential for using the LS method in cloud and mesoscale models is being explored. In addition, a computationally less intensive formulation of the LS method is being developed. Nevertheless, if the current LS method is applied only to velocity fields in a three-dimensional model with complex physics (e.g., detailed radiation and cloud and precipitation physics), the cost increase of using the method is on the order of about 15%. Finally, a number of different dealiasing filters to control the spectral blocking phenomena and weak spurious aliasing are being examined. These developments and issues will be addressed in future papers.

Acknowledgments. Thanks are due to Ms. Kathy Kanak, Dr. Gregory Tripoli, Dr. Louis Wicker, and Dr. Robert Wilhelmson for their helpful comments and discussions. We also thank the reviewers for their excellent comments. The first author was supported, in part, by the Center for Analysis and Prediction of Storms (CAPS), which is funded by the National Science Foundation.

APPENDIX A

The LS Method and Filter Coefficients Based on Lagrange Polynomials

A89 demonstrated the capabilities of the LS method using the one-dimensional advection–diffusion equation:

$$\frac{\partial u_i}{\partial t} = u_i \frac{\partial u_i}{\partial x} + \nu \frac{\partial^2 u_i}{\partial x^2} \quad \text{with} \quad i = 1, N, \quad \text{(A1)}$$

where ν is the kinematic viscosity and N is the number of grid points. This equation was solved with the LS method using the following algorithmic structure (see Fig. 1):

$$\frac{\partial u_i}{\partial t} = \text{LIN}_i + \text{NLIN}_i \quad \text{with} \quad i = 1, N \quad \text{(A2)}$$

$$\text{LIN}_i = \nu \sum_{k=-R}^{R} [D_k^{(2)} u_{i+k}] \quad \text{(A3)}$$

$$\text{NLIN}_i = \sum_{k=-2R}^{2R} [T_k A(u_{2i+k})] \quad \text{(A4)}$$

$$A(u_{i2}) = -U_{i2} \sum_{k=-2R}^{2R} [D_k^{(1)} u_{(i2+k)/2}] \quad i2 = 1, 2N$$

(ignoring terms where $i2 + k$ is odd) (A5)

$$U_{i2} = \sum_{k=-2R}^{2R} [L_k u_{(i2+k)/2}]$$

(ignoring terms where $i2 + k$ is odd). (A6)

In (A2)–(A6), LIN is the linear term, NLIN is the nonlinear term, $A(u)$ is the advection of u, and U is the u velocity on a double-density grid. The first derivative, second derivative, truncation (dealiasing), and interpolation coefficients are $D_k^{(1)}$, $D_k^{(2)}$, T_k, and L_k, respectively.

The order of an LS model is limited primarily by the length and order of accuracy of the interpolation, differentiation, and truncation filters. In general, an LS model with a filter length of $2R$ can be considered to be analogous to an N-order FD model. One example for the design of interpolation, first and second derivative, and truncation–low-pass filters that are appropriate for use in LS models is discussed by A89. While A89's filters are formally second-order accurate, the phase speed characteristics for his $2R = 10$th-order derivative filter are similar to those for a 10th-order finite-difference scheme, and in fact, slightly better at shorter wavelengths. As an alternative to the filters described by A89, the design of $2R = N$-order accurate filters based on Lagrange polynomials for constant and nonconstant grid spacing are described below following Purser and Leslie (1988, hereafter referred to as PL88). Without the dealiasing filters, this version of LS method collapses to a standard high-order Taylor series FD method. When filter lengths span the integration domain and the dealiasing stage is retained, the LS method becomes an ST method (A89).

The first step in implementing the LS method is interpolating model state fields to a high-resolution grid. For the sake of simplicity, we use a double-density high-resolution grid (denoted by the index $i2$). The Lagrange interpolation coefficients, $L_k(x_{i2})$, for a $2R$-degree scheme assuming arbitrary grid spacing to interpolate

variables from original model grid locations x_i to high-resolution grid locations x_{i2} is given by

$$L_k(x_{i2}) = \prod_{\substack{k=-(R-1) \\ k\neq 0}}^{R} \left(\frac{x_{i2} - x_i}{x_{i+k} - x_i}\right), \qquad \text{(A7)}$$

where k is the index of the filter coefficient and $2R$ is the degree of the filter. No interpolations are required to put variables from the original model grid onto the high-resolution grid where locations on the two grids correspond exactly. For equal grid spacing, the Lagrange interpolation filter coefficients for midpoint interpolation can be defined, following PL88, as

$$L_k(x_{i2}) = \frac{(-)^{k-0.5}}{k}\frac{\beta_k}{\pi}$$

$$\text{for} \quad k = \pm\frac{1}{2}, \pm\frac{3}{2}, \cdots, \pm\left(R - \frac{1}{2}\right)$$

$$\text{with} \quad L_k(x_{i2}) = L_{-k}(x_{i2}). \qquad \text{(A8)}$$

The parameter β_k is defined by PL88 as

$$\beta_k = \frac{(R!)^2}{(R+k)!(R-k)!}. \qquad \text{(A9)}$$

Equivalently, and more conveniently in the case of the half-integer values of R and k needed in midpoint interpolation, the parameter β_k can be defined by

$$\frac{\beta_k}{\pi} = \left[\frac{(2R)!}{2^{(2R)}(R-0.5)!}\right]^2 \frac{1}{(R+k)!(R-k)!}. \qquad \text{(A10)}$$

With equal-spaced grids, interpolation to a grid with twice the resolution of the original model grid requires only interpolation for grid points that are halfway between the original model grid points. A diagram of the model grid points used in the interpolation for equal-spaced grids with the LS method is shown in Fig. A1. The interpolation of a state variable $\phi(x_{i2})$ is accomplished with

$$\phi(x_{i2}) \approx \sum_{k=-R}^{R} [L_k(x_{i2})\phi(x_{i+k})]. \qquad \text{(A11)}$$

The first-derivative coefficients $D_k^{(1)}(x_{i2})$ for a $2R$-order scheme can be obtained by taking the first derivative of the Lagrange interpolation polynomial (A7):

$$D_k^{(1)}(x_{i2}) = \frac{\partial L_k(x_{i2})}{\partial x}. \qquad \text{(A12)}$$

As before, only information on the original model grid is used to compute the derivatives for the LS method (A89). For equally spaced grids, the first-derivative coefficients using Lagrange polynomials for high-resolution grid locations that correspond exactly with original model grid locations (see Fig. A1) are given, following PL88, as standard finite differences for unstaggered grids:

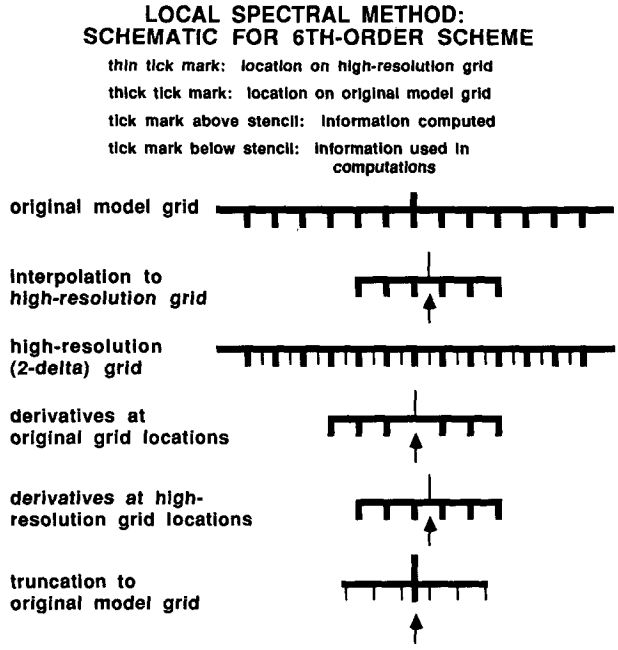

FIG. A1. Schematic of the application of interpolation, differencing, and truncation filters in local spectral models. Bold tick marks represent locations on the original model grid, and thin tick marks are locations on the high-resolution grid. In general, tick marks represent grid points used in calculations such as interpolation, differentiation, or truncation. Arrows point to locations of the results from the required calculations.

$$D_k^{(1)}(x_{i2}) = -\frac{(-)^k}{k}\beta_k \quad \text{for} \quad k = \pm 1, \cdots, \pm R$$

$$\text{with} \quad D_k^{(1)}(x_{i2}) = -D_{-k}^{(1)}(x_{i2}). \qquad \text{(A13)}$$

The first-derivative coefficients for high-resolution grid locations that are midway between original model grid locations (see Fig. A1) are given, following PL88, as standard finite differences for staggered grids:

$$D_k^{(1)}(x_{i2}) = -\frac{(-)^{k-0.5}}{k^2}\frac{\beta_k}{\pi}$$

$$\text{for} \quad k = \pm\frac{1}{2}, \pm\frac{3}{2}, \cdots, \pm\left(R - \frac{1}{2}\right)$$

$$\text{with} \quad D_k^{(1)}(x_{i2}) = -D_{-k}^{(1)}(x_{i2}). \qquad \text{(A14)}$$

Using the first-derivative coefficients, the derivative of $\phi(x_{i2})$ is

$$\frac{\partial\phi(x_{i2})}{\partial x} \approx \frac{1}{\Delta x}\sum_{k=-R}^{R} [D_k^{(1)}(x_{i2})\phi(x_{i+k})]. \qquad \text{(A15)}$$

The second-derivative coefficients $D_k^{(2)}(x_{i2})$ can be computed by taking the second derivative of the Lagrange interpolation polynomial (A7):

$$D_k^{(2)}(x_{i2}) = \frac{\partial^2 L_k(x_{i2})}{\partial x^2}. \qquad \text{(A16)}$$

For equally spaced grids, the second-derivative coefficients can be defined, following PL88, as

$$D_k^{(2)}(x_{i2}) = -\frac{(-)^k}{k^2} 2\beta_k \quad \text{for} \quad k = \pm 1, \cdots, \pm R$$

$$\text{with} \quad D_k^{(2)}(x_{i2}) = D_{-k}^{(2)}(x_{i2}), \quad \text{(A17)}$$

with

$$D_0^{(2)}(x_{i2}) = -\sum_{\substack{k=-R \\ k\neq 0}}^{R} D_k^{(2)}(x_{i2}). \quad \text{(A18)}$$

As with the first derivative, the second derivative of $\phi(x_{i2})$ is computed as

$$\frac{\partial^2 \phi(x_{i2})}{\partial x^2} \approx \frac{1}{\Delta x^2} \sum_{k=-R}^{R} [D_k^{(2)}(x_{i2})\phi_k]. \quad \text{(A19)}$$

In practice, the linear diffusion terms can be evaluated on either the high-resolution grid or original model grid. For nonlinear diffusion terms, taking the first derivative of the product of the first derivatives and an appropriate mixing coefficient is appropriate.

The truncation filter is used to project the nonlinear tendencies on the high-resolution grid back to the original model grid (Fig. A1). In practice, the truncation filter is similar to a low-pass filter. The family of linear filters described by Purser (1987) is both versatile and simple. These filters, with coefficients denoted as T_k, have arbitrary cutoff frequencies controlled by parameters R and S, where R controls the roll-off of the filter and S controls the smoothness of the filter response at the grid scale (see, for example, Purser 1987; Shapiro 1970; Shuman 1957). The spectral responses of these filters are shown in Purser (1987). (A89 also shows an example of the spectral response for his filter, which is based on digital filtering techniques.) In the case of $(R, S) = (R, 0)$, the truncation coefficients T_k can be obtained from Lagrange interpolation coefficients by

$$T_k(x_{i2}) = 0.5 L_k(x_{i2}), \quad \text{with} \quad T_{k=0}(x_{i2}) = 0.5,$$

$$\text{and} \quad T_{-k}(x_{i2}) = T_k(x_{i2}). \quad \text{(A20)}$$

Truncated advection tendencies are computed, for example, as

$$A(u_i) \approx \sum_{k=-R}^{R} [T_k A(u_{i2+k})]. \quad \text{(A21)}$$

Truncation filter coefficients of the form in (A20) were used in the test simulations described in this paper. While no problems have been encountered with these coefficients, there is a very small amount of aliasing leakage. Filters with a slightly lower cutoff frequency can help control this leakage; however, they might result in excessive smoothing of solutions in low-order models. In some cases, though, additional smoothing might be desirable.

APPENDIX B

Linear Stability of the LS Method

The linear stability for a $2R$-order LS scheme is assumed to be at least the same as the linear stability for an N-order FD scheme if $2R = N$. The linear stability of an N-order FD scheme can be computed following Haltiner and Williams (1980). For example, consider the N-order advection equation

$$\Phi_{m,n+1} - \Phi_{m,n-1} = -c \sum_{i=1}^{N/2} a_i(\Phi_{m+i,n} - \Phi_{m-i,n}), \quad \text{(B1)}$$

where Φ is the quantity advected, m is the space index, n is the time index, a_i are the difference coefficients, and c is a constant phase speed advecting Φ. Assume a solution of the form

$$\Phi_{m,n} = A \exp(i\alpha n\Delta t - i\mu m\Delta x), \quad \text{(B2)}$$

and substitute it into the difference equation. The resulting equation is

$$\sin(\alpha\Delta t) = \frac{c\Delta t}{\Delta x} \sum_{m=1}^{N/2} [a_i \sin(m\mu\Delta x)]. \quad \text{(B3)}$$

For real α, the magnitude of the right-hand side of this equation must be less than or equal to one for linear stability. The maximum magnitude of the right-hand side of the (B3) is found by taking the derivative with respect to $\mu\Delta x$, setting the result to zero, and finding the real root of the polynomial. The derivative is given as

$$\sum_{m=1}^{N/2} [a_i m \cos(m\mu\Delta x)] = 0.0, \quad \text{(B4)}$$

and trigonometric identities are used to form an equation in terms of powers of cosines. The real root $R = m\mu\Delta x$ is found using Newton–Raphson iterations. After the root is found, $\mu\Delta x = \cos^{-1}(R)$ is solved. Then $\mu\Delta x$ is substituted into (B3), and the value of the right-hand side of (B3) is found. From this, the Courant number is given as

$$\left| \frac{c\Delta t}{\Delta x} \sum_{m=1}^{N/2} [a_i \sin(m\mu\Delta x)] \right| \leq 1. \quad \text{(B5)}$$

The stability criterion for 2d-, 4th-, 6th-, 8th-, and 10th-order finite-difference schemes is shown in Table B1.

TABLE B1. Courant numbers for second-order centered-in-time and N-order centered-in-space difference schemes in one dimension.

Scheme order	Courant number
02	1.0000
04	0.7287
06	0.6273
08	0.5727
10	0.5383

The Courant number for two and three dimensions is that for one dimension divided by $2^{0.5}$ and $3^{0.5}$, respectively.

REFERENCES

Anderson, J. R., 1989: A local, minimum aliasing method for use in nonlinear numerical models. *Mon. Wea. Rev.*, **117,** 1369–1379.

——, K. K. Droegemeier, and R. B. Wilhelmson, 1986: Simulation of the thunderstorm subcloud environment. Preprints, *14th Conf. on Severe Local Storms,* Indianapolis, IN, Amer. Meteor. Soc., 147–150.

Arakawa, A., 1966: Computational design for long-term numerical integrations of the equations of atmospheric motions. *J. Comput. Phys.*, **1,** 119–143.

——, and V. R. Lamb, 1977: Computational design of the basic dynamical processes of the UCLA general circulation model. *Methods of Computational Physics,* Vol. 17, Academic Press, 174–265.

Asselin, R., 1972: Frequency filter for time integrations. *Mon. Wea. Rev.*, **100,** 487–490.

Boyd, J. P., 1991: Sum-accelerated pseudospectral methods: The Euler-accelerated sinc algorithm. *Appl. Numer. Math.*, **7,** 287–296.

Chen, X-S, 1991: The aliased and the de-aliased spectral models of the shallow water equations. Preprints, *9th Conf. on Numerical Weather Prediction,* Denver, CO, Amer. Meteor. Soc., 819–822.

Chorin, A. J., 1967: A numerical method for solving incompressible flow problems. *J. Comput. Phys.*, **2,** 12–16.

Clark, T. L., 1979: Numerical simulations with a three-dimensional cloud model: Lateral boundary condition experiments and multicellular severe storm simulations. *J. Atmos. Sci.*, **36,** 2191–2215.

Conte, S. D., and C. de Boor, 1980: *Elementary Numerical Analysis. An Algorithmic Approach.* 3d ed. McGraw-Hill, 432 pp.

Droegemeier, K. K., and R. B. Wilhelmson, 1986: Kelvin–Helmholtz instability in a numerically simulated thunderstorm outflow. *Bull. Amer. Meteor. Soc.*, **67,** 416–417.

——, and ——, 1987: Numerical simulation of thunderstorm outflow dynamics. Part 1: Outflow sensitivity experiments and turbulence dynamics. *J. Atmos. Sci.*, **44,** 1180–1210.

Fishcer, P. F., 1990: Analysis and application of a parallel spectral element method for the solution of the Navier–Stokes equations. *Comput. Methods Appl. Mech. Eng.*, **80,** 483–492.

Haltiner, G. J., and R. T. Williams, 1980: *Numerical Prediction and Dynamic Meteorology.* 2d ed. John Wiley and Sons, 477 pp.

Kaplan, M. L., J. W. Zack, V. C. Wong, and J. J. Tuccillo, 1982: Initial results from a mesoscale atmospheric simulation system and comparison with the AVE-SESAME I data set. *Mon. Wea. Rev.*, **110,** 1564–1590.

Klemp, J. B., and R. B. Wilhelmson, 1978: The simulation of three-dimensional convective storm dynamics. *J. Atmos. Sci.*, **35,** 1070–1096.

Kurihara, Y., and J. Holloway, 1967: Numerical integrations of a nine-level global primitive equation model formulated by the box method. *Mon. Wea. Rev.*, **118,** 586–612.

Machenhauer, B., and E. Rasmussen, 1972: On the integration of the spectral hydrodynamical equation by a transform method. Report No. 3 Institut for Teoretisk Meteorolgi, Kobenhavns Universitet, Denmark, 44 pp.

Matsuno, T., 1966: Numerical integrations of primitive equations by use of a simulated backward difference method. *J. Meteor. Soc. Japan,* **44,** 76–84.

Oppenheim, A. V., and R. W. Schafer, 1975: *Digital Signal Processing.* Prentice-Hall, 585 pp.

Orszag, S. A., 1970: Transform method for the calculation of vector-coupled sums: Application to the spectral form of the vorticity equation. *J. Atmos. Sci.*, **27,** 890–895.

——, 1971: On the elimination of aliasing in finite-difference schemes by filtering of high-wavenumber components. *J. Atmos. Sci.*, **28,** 1074.

Papoulis, A., 1959: Minimum-bias windows for high-resolution spectral estimates. *IEEE Trans. Inf. Theory,* **IT-19,** 9–12.

Phillips, N. A., 1959: An example of nonlinear computational instability. *The Atmosphere and Sea in Motion, Rossby Memorial Volume,* Rockefeller Institute Press, 509 pp.

Purser, R. J., 1987: The filtering of meteorological fields. *J. Appl. Meteor.*, **26,** 1764–1769.

——, and L. M. Leslie, 1988: A semi-implicit, semi-Lagrangian finite difference scheme using high order differencing on a nonstaggered grid. *Mon. Wea. Rev.*, **116,** 2069–2080.

Shapiro, R., 1970: Smoothing, filtering and boundary effects. *Rev. Geophys. Space Phys.*, **8,** 359–387.

Shuman, G., 1957: Numerical methods in weather prediction. 2: Smoothing and filtering. *Mon. Wea. Rev.*, **85,** 357.

Straka, J. M., R. B. Wilhelmson, L. J. Wicker, K. K. Droegemeier, and J. R. Anderson, 1991: Workshop on numerical methods for solving nonlinear flow problems. Preprints, *Ninth Conf. on Numerical Weather Prediction,* Denver, CO, Amer. Meteor. Soc., 274–278.

——, ——, ——, J. R. Anderson, and K. K. Droegemeier, 1993: Numerical solutions from simulations of a nonlinear density current. *Int. J. Num. Methods Fluids,* in press.

Takacs, L. L., 1985: A two step scheme for the advection equation with minimized dissipation and dispersion errors. *Mon. Wea. Rev.*, **113,** 1050–1065.

Tremback, C. J., J. Powell, W. R. Cotton, and R. A. Pielke, 1987: The forward-in-time upstream advection scheme: Extensions to higher orders. *Mon. Wea. Rev.*, **115,** 540–555.

Van der Houwen, P. J., B. P. Sommeijer, and F. W. Wubs, 1990: Analysis of smoothing operators in the solution of partial differential equations by explicit difference schemes. *Appl. Numer. Math.*, **6,** 501–521.